Three-dimensional numerical simulation of stepped dropshaft with different step shapes

Jingkang Sun, Shangtuo Qian, Hui Xu, Xiaosheng Wang and Jiangang Feng

ABSTRACT

The deep tunnel system is increasingly used worldwide for stormwater conveyance and storage, providing a robust and effective means of preventing urban waterlogging. In the system, the dropshaft, with the function of conveying stormwater to the deep tunnels underground, often runs under conditions of high falling head and large discharge. Based on the standard stepped dropshaft, a blade-shaped stepped dropshaft was proposed in order to control the potential standing wave and improve discharge capacity. Its hydraulic characteristics in respect of flow pattern, flow rate distribution, time-averaged pressure and energy dissipation were investigated by numerical simulation. Compared with the standard stepped dropshaft, the blade-shaped stepped dropshaft generated a more uniform flow rate distribution in the radial direction, therefore effectively decreasing the height of the standing wave near the external wall. The negative pressure areas that easily existed on the vertical wall of steps were well controlled. The energy dissipation of the blade-shaped stepped dropshaft was as high as that of the standard stepped dropshaft. Therefore, the blade-shaped stepped dropshaft could be a preferable design for the deep tunnel system.

Key words | blade-shaped, hydraulic characteristic, numerical simulation, stepped dropshaft

Jingkang Sun
College of Water Conservancy and Hydropower
  Engineering,
Hohai University,
Nanjing 210098,
China

Shangtuo Qian (corresponding author)
Hui Xu
Xiaosheng Wang
Jiangang Feng
College of Agricultural Science and Engineering,
Hohai University,
Nanjing 210098,
China
E-mail: qshttc@163.com

HIGHLIGHTS

- Report a new kind of stepped dropshaft in deep tunnel systems, namely the blade-shaped stepped dropshaft.
- Obtain the hydraulic characteristics of the blade-shaped stepped dropshaft in respect of flow pattern, flow rate distribution, time-averaged pressure and energy dissipation.
- Compare with the standard stepped dropshaft to obtain the influence of the step shape on the hydraulic characteristics.

INTRODUCTION

With the rapid development of urbanization, the increase of population and the decrease of water area have led to great pressure on the sewer and storage tunnels of the city (Vasconcelos & Wright 2006). Due to global climate change, the pressure may further increase with frequent intense rain events leading to urban water problems such as waterlogging (Zhang *et al.* 2016). Deep storage tunnel systems, generally including several dropshafts and underground tunnel, can be effective in preventing the urban water problems, and have been implemented or is under consideration in many cities (Guo & Song 1990; Changnon 2010). In this system, the stormwater runoff can be diverted to the deep tunnels through dropshafts, and then diverted to the river or sewage plant, or temporarily stored in the

tunnels (Guo & Song 1991). The dropshaft often runs with the conditions of high falling head and large discharge, which may lead to operational issues related to energy dissipation and cavitation, and even cause disasters like geysers (Rajaratnam *et al.* 1997; Vasconcelos & Wright 2011). Therefore, it is important to take into account the hydraulic characteristics in the dropshaft.

Dropshafts can be divided into four typical types: the vortex dropshaft, baffle dropshaft, plunging dropshaft and helicoidal-ramp dropshaft (He *et al.* 2017). Previous research indicated that the helicoidal-ramp dropshaft shows a better performance for high falling head and large discharge with good energy dissipation and exhaust effect (Kawasaki *et al.* 1999). It includes a vertical circular dropshaft and a continuous helicoidal ramp attached to the dropshaft wall. The water can skim down along the ramp, and the air can be released from the center hollow column without any extra ventilation device (Ansar & Jain 1997). The energy dissipation occurs as distributed friction loss along the helicoidal ramp without any extra energy dissipators (Kennedy *et al.* 1988).

Inspired by the helicoidal-ramp dropshaft, Wu *et al.* (2018) proposed a stepped dropshaft in order to provide well aeration to decrease the risk of cavitation erosion and to further increase the energy dissipation. Figure 1(a) is a definition sketch of the standard stepped dropshaft. By changing the ramps to successive steps, the flow skimming over the ramps could be converted to successive nappes impacting steps with vortices beneath them. On the one hand, the energy dissipation can increase due to nappe breakup in the air and impact on the steps as well as full or partial hydraulic jumps. On the other hand, the intense turbulence resulting from the vortice increases the self-aeration from the free surface, which can decrease the risk of cavitation.

Some investigations have been focused on the hydraulic characteristics of the stepped dropshaft. Wu *et al.* (2018) indicated that there are two typical flow regimes in the stepped dropshaft: nappe flow and skimming flow, which are similar to that in the stepped spillway (Qian & Wu 2020; Wu *et al.* 2020). Compared with the stepped spillway, the flow affected under the centrifugal force is more complicated for the stepped dropshaft. Wu *et al.* (2017) showed that the height of the standing wave near the external wall decreases with the increase in the approach flow Froude number, but increases with the increase in the curvature of the dropshaft. The influence of the geometric parameter of the stepped dropshaft on the hydraulic characteristics has been investigated by a few authors. Qi *et al.* (2018) and Liao *et al.* (2019) analyzed the influence of step rotation angles on the flow patterns by numerical simulation. The results showed that with the increase in the step rotation angles, the maximum water depth on the step initially decreases and then increases, but the location of the maximum water depth is opposite. Shen *et al.* (2019) studied the influence of end sills on the energy dissipation of the stepped dropshaft. The results showed that the end sills on the steps can increase the energy dissipation but decrease the discharge capacity of the stepped dropshaft.

The standing wave, as an important flow phenomenon, is associated with the discharge capacity. When the height of the standing wave is too large to touch the bottom of the upper step, the discharge capacity of the stepped dropshaft will be limited. Therefore, it is necessary to control
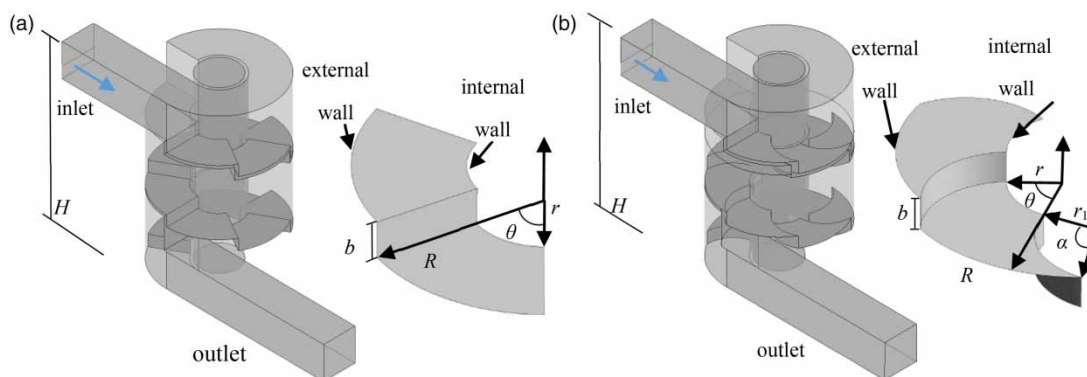

Figure 1 | The stepped dropshaft: (a) standard; (b) blade-shaped.

the height of the standing wave and improve the discharge capacity. In this study, a new design of stepped dropshaft is proposed, namely the blade-shaped stepped dropshaft (Figure 1(b)). By modifying the vertical wall of the step to a curved vertical wall, it generates a more uniform flow rate distribution along the radial direction, therefore controlling the standing wave and improving the discharge capacity. ANSYS CFX 17.0 was used to simulate the flow in the stepped dropshaft. The main objectives of this study are: (1) to obtain the hydraulic characteristics of the blade-shaped stepped dropshaft in respect of flow pattern, flow rate distribution, time-averaged pressure and energy dissipation; (2) to compare with the standard stepped dropshaft and obtain the influence of the step shape on the hydraulic characteristics.

NUMERICAL SIMULATION

Model setup

Figure 1 is the definition sketch of the stepped dropshaft, which consisted of a vertical circular shaft with a tangential horizontal inlet channel and outlet channel. Air can be released through the air holes arranged on the internal wall below the steps. For both the standard and blade-shaped stepped dropshafts, the height (H) of the dropshaft, the radius (R) of the external wall, the radius (r) of the internal wall, the height (b) and step rotation angle (θ) of each step were the same: $H = 1.5$ m, $R = 0.5$ m, $r = 0.2$ m, $b = 0.1$ m, and $\theta = 60°$. Compared with the standard stepped dropshaft, the vertical wall of the step was modified to be a curved vertical wall for the blade-shaped stepped dropshaft. The step rotation angle (α) and the radius (r_1) of the curved vertical wall were $\alpha = 86°$ and $r_1 = 0.25$ m, respectively. The length of the inlet and outlet channels was 1 m and 1.5 m, respectively. The cross section of the inlet and outlet channels was rectangular with 0.3 m width and 0.3 m height, respectively.

Volume of fluid method

The volume of fluid method (VOF) model is suitable to model the free-surface flow and track the volume fraction of each fluid over the entire region (Hirt & Nichols 1981; Qian *et al.* 2019). The sum of the volume fractions of water and gas in each of the calculated grid cells is constant, and they are expressed as α_w and α_a, respectively:

$$\alpha_w + \alpha_a = 1 \tag{1}$$

The density ρ and the viscosity μ can be expressed as:

$$\rho = \alpha_w \rho_w + (1 - \alpha_w)\rho_a \tag{2}$$

$$\mu = \alpha_w \mu_w + (1 - \alpha_w)\mu_a \tag{3}$$

where ρ_w and ρ_a are the density of water and gas, respectively; μ_w and μ_a are the viscosity of water and gas, respectively.

The variables and their attributes represent air or water, or a mixture of them at any control volume. The tracking of the interface between air and water is accomplished by the continuity equation as follows:

$$\frac{\partial \alpha_w}{\partial t} + u_i \frac{\partial \alpha_w}{\partial x_i} = 0 \tag{4}$$

where x_i and u_i are the coordinates and velocity components, respectively ($i = 1, 2, 3$), t is the time.

Turbulence model

The shear stress transport rotation-curvature correction (SST-CC) model can provide an accurate prediction of the swirling flow evolution and the boundary layer simulations, which are relevant to the flow characteristics in the stepped dropshaft (Menter 1994). Many papers have simulated the complicated hydraulic properties related to the swirling flow and high accuracy boundary layer using the SST-CC model (Guo *et al.* 2018). Therefore, the SST-CC model can be used to model the flow in the stepped dropshaft. The governing equations are as follows:

$$\mu_T = \rho \frac{k}{\omega} \tag{5}$$

$$\frac{\partial \rho k}{\partial t} + \frac{\partial (\rho u_j k)}{\partial x_j} = P_k f_{r1} - \beta * \rho \omega k + \frac{\partial}{\partial x_j}\left(\left(\mu + \frac{\mu_T}{\sigma_k}\right)\frac{\partial k}{\partial x_j}\right) \tag{6}$$

$$\frac{\partial \rho \omega}{\partial t} + \frac{\partial(\rho u_j \omega)}{\partial x_j} = \frac{\rho P_\omega}{\mu_T} f_{r1} - \rho \beta \omega^2 + 2(1 - f_1) \frac{\rho \sigma_{\omega 2}}{\omega} \frac{\partial k}{\partial x_j} \frac{\partial \omega}{\partial x_j}$$
$$+ \frac{\partial}{\partial x_j} \left((\mu + \frac{\mu_T}{\sigma_\omega}) \frac{\partial \omega}{\partial x_j} \right) \tag{7}$$

$$f_1 = \tanh \left\{ \min \left[\max \left(\frac{\sqrt{k}}{0.09 \omega d}, \frac{500\mu}{\rho \omega d^2} \right), \frac{4 \rho \sigma_{\omega 2} k}{CD_{k\omega} d^2} \right] \right\} \tag{8}$$

$$CD_{k\omega} = \max \left(2 \frac{\rho \sigma_{\omega 2}}{\omega} \frac{\partial k}{\partial x_j} \frac{\partial \omega}{\partial x_j}, 10^{-20} \right) \tag{9}$$

where ω = specific dissipation rate, k = turbulent kinetic energy, μ_T = turbulent eddy viscosity, d = the distance to the nearest wall, and P_k and P_ω = production terms. β, β^*, σ_k, σ_ω and $\sigma_{\omega 2}$ are the model coefficients.

The curvature correction term (f_{r1}) can increase the sensitivity to the curvature and rotation of the streamline, which is more in line with the spiral bending flow of the water flow inside the dropshaft (Spalart & Shur 1997). The empirical formula ($f_{rotation}$) for curvature correction is:

$$f_{rotation} = (1 + C_{r1}) \frac{2r*}{1 + r*} [1 - C_{r3} \tan^{-1}(C_{r2} \tilde{r}) - C_{r1}] \tag{10}$$

$$f_{r1} = \max [\min (f_{rotation}, 1.25), 0] \tag{11}$$

where the constant parameters are $C_{r1} = 1.0$, $C_{r2} = 2.0$, $C_{r3} = 1.0$. $r*$ and $\tilde{r}$ are related to the strain rate tensor (S) and the magnitude of vorticity (Ω):

$$r* = \frac{S}{\Omega} \tag{12}$$

$$\tilde{r} = 2\Omega_{ik} S_{jk} \left[\frac{DS_{ij}}{Dt} + (\varepsilon_{imn} S_{jn} + \varepsilon_{jmn} S_{in}) \Omega_m^{rot} \right] \frac{1}{\Omega D^3} \tag{13}$$

$$D = \max (S^2, 0.09\omega^2) \tag{14}$$

Numerical algorithm

The Geo-Reconstruct can obtain the face fluxes whenever a cell is filled with water or air and be used when the cell is near the interface between two phases (Cui *et al.* 2020). It represents the interface between fluids using a piecewise-linear approach. The Pressure-Implicit with Splitting of Operators (PISO) algorithm, based on the higher degree of the approximate relation between the corrections for pressure and velocity, can decrease the number of iterations required for convergence, especially for transient problems (Xie & Xiao 2017).

Model grid, boundary and initial conditions

The mesh of the numerical model was configured as a structural grid with 2290037 hexahedral grid cells. Mesh refinement was used near the stepped dropshaft wall to deal with the swirling flow attached to the wall. The minimum grid size near the dropshaft wall was 2 mm. Mesh convergence was tested using a coarser mesh with 1648431 cells, showing less than 5% difference to the predicted average velocity and time-averaged pressure at the end of the eleventh step.

The upstream inlet was assumed to be the mass flow bulk. The downstream outlet was assumed to be the pressure outlet and a static pressure equal to zero was assumed over it. The top of the central hollow was assumed to be the opening boundary condition with a relative pressure equal to zero, which allows the air to cross the boundary either into or out of the domain. The wall boundary was assumed to be the no-slip wall.

The dimensionless flow rate is $Q^* = Q/(g(R - r)^5)^{1/2}$, where Q is the flow rate, g is the acceleration of gravity. Numerical predictions were carried out for the range of the flow rates was $Q = 0.012$–0.048 m³/s, which corresponded to $Q^* = 0.078$–0.311. The minimum time step was 0.001s and the max iterations per time step were set as 20.

Model validation

The experiment results (Wu *et al.* 2018) were used to evaluate the simulated settings to verify the accuracy of the calculation. In the experiment dropshaft, $b = 0.131$ m, $\theta = 150°$, $R = 0.25$ m, $r = 0.1$ m, $Q^* = 0.13$ and 0.42. Figure 2 shows the time-averaged pressure p on the ninth step horizontal surface in the flow direction and the radial direction, where x is the position of the measuring points from the vertical wall along the flow direction; L_X is the length from the vertical wall along the arranged line of the measuring points; y is the location of the measuring points
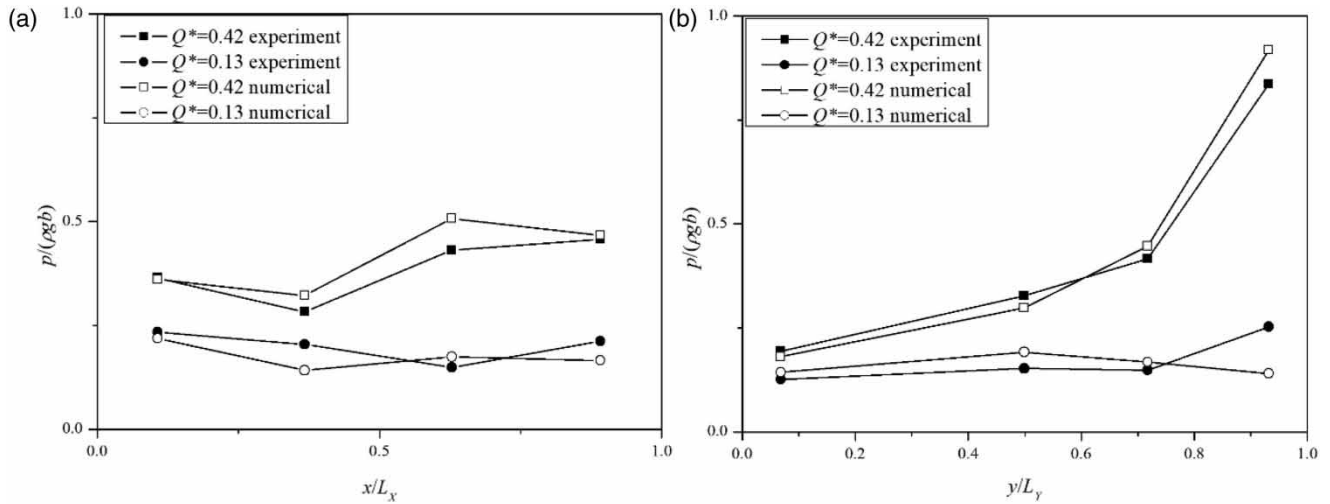
Figure 2 | Time-averaged pressure obtained by numerical simulation and experiment: (a) in the flow direction; (b) in the radial direction.

from the internal wall along the radial direction; and L_Y is the length from the internal wall to the external wall along the radial direction.

Figure 2 showed that the maximum relative deviations in the flow and radial direction are 4.30% and 2.04%, respectively. This indicated that the results of the numerical simulation agree well with the experiment.

RESULTS AND DISCUSSION

Flow pattern

Under the influence of centrifugal force, the flow behaviors on each step of the stepped dropshaft vary in the radial direction, with the main flow remaining near the external wall. According to the variations of the main flow, referring to the flow regime classification for the stepped spillway, the flow patterns of the stepped dropshaft can be classified into nappe and skimming flows. The nappe flow is characterized by a succession of falling jets, the presence of air cavities beneath them, and hydraulic jumps downstream of the falling jets. The energy of the nappe flow is mainly dissipated by the impact of the falling jets, and the turbulence of the hydraulic jump. The characteristic of the skimming flow is that the flow skims over the steps as a coherent stream and is cushioned by the recirculating fluid trapped on the steps. The energy of the skimming flow is mainly dissipated

by the intense turbulent momentum exchange between the mainstream and the recirculation.

Figure 3 shows the flow patterns of both stepped dropshafts at $Q^* = 0.078$ and 0.155. For the standard stepped dropshaft, the nappe flow exists at $Q^* = 0.078$ and 0.155. For the blade-shaped stepped dropshaft, the nappe flow exists at $Q^* = 0.078$ and the skimming flow exists at $Q^* = 0.155$. Therefore, the flow rate required for the skimming
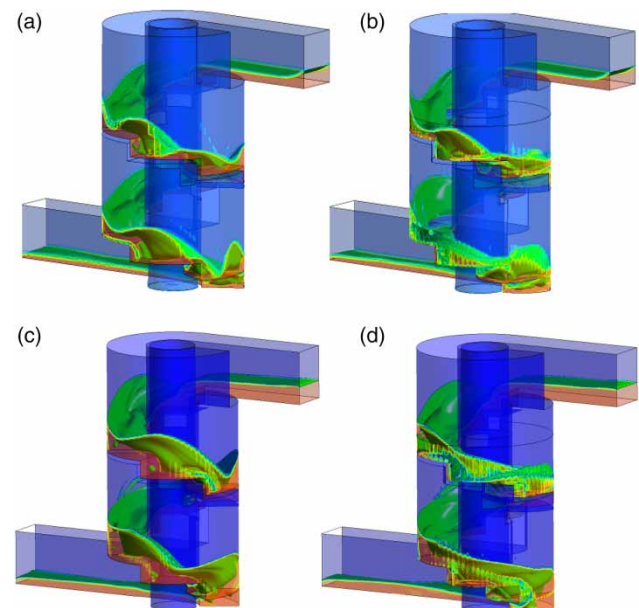

Figure 3 | Flow patterns: (a) and (c) $Q^* = 0.078$ and 0.155 for standard stepped dropshaft; (b) and (d) $Q^* = 0.078$ and 0.155 for blade-shaped stepped dropshaft.

flow in the blade-shaped stepped is significantly less than that in the standard stepped dropshaft.

Figure 3(a) and 3(b) highlight similar nappe flow performance in both dropshafts. Different from the stepped spillway, the falling jets impact on the step near the external wall under the effect of the centrifugal force, and standing waves are generated due to the deflection of the falling jets. For the standard stepped dropshaft, with the increase of Q^*, the jet length of the nappe flow increases gradually, resulting in the jet flow jumping over the adjacent step and landing on the lower step (Figure 3(c)). For the blade-shaped stepped dropshaft, $Q^* = 0.155$ is large enough for generating the skimming flow, with the presence of the water surface streamline parallel to the pseudo-bottom and the absence of standing waves and air cavities (Figure 3(d)).

Flow rate distribution

Figure 3 shows that the flow is fully developed from the eighth step at $Q^* = 0.155$. Figure 4 shows the flow rate distribution q/Q with y/L_Y in the cross sections at the end of the eighth to the eleventh steps at $Q^* = 0.155$, where q is the flow rate integration along the water depth. For both stepped dropshafts, q/Q increases from internal to external owing to the influence of centrifugal force and decreases near the external wall owing to the sidewall resistance. The maximum q/Q is 0.231 and 0.112 at $y/L_Y = 0.95$ for the standard stepped dropshaft and the blade-shaped stepped dropshaft, respectively. For the

standard stepped dropshaft, with increasing y/L_Y, q/Q rises slowly at $0 < y/L_Y < 0.5$ but surges at $0.5 < y/L_Y < 0.95$. For the blade-shaped stepped dropshaft, q/Q rises more slowly as a cross wavy line with increasing y/L_Y; therefore, the distribution of q/Q is more uniform with the maximum about half of that in the standard stepped dropshaft.

It can be found that the distribution of q/Q shows periodic on different steps. q/Q on the eighth and tenth steps are similar, and the q/Q on the ninth and eleventh steps are similar. For the standard stepped dropshaft, q/Q of the eighth and tenth steps are greater than that of the ninth and eleventh steps at $0.5 < y/L_Y < 1$, which is opposite at $0 < y/L_Y < 0.5$. For the blade-shaped stepped dropshaft, q/Q rises as a cross wavy line shape: when $0 < y/L_Y < 0.2$ and $0.5 < y/L_Y < 0.8$, q/Q of the eighth and tenth steps are greater than that of the ninth and eleventh steps; when $0.2 < y/L_Y < 0.5$ and $0.8 < y/L_Y < 1$, it is just the opposite.

Figure 5 shows the flow rate difference $\Delta q/Q$ between the internal wall and external wall, where Δq is the average flow rate difference between the internal wall and external wall from the eighth to eleventh steps. It shows that the relations between $\Delta q/Q$ and Q^* are linear in both dropshafts. Due to the influence of centrifugal force, the $\Delta q/Q$ gradually increases with the increase of Q^*. Obviously, $\Delta q/Q$ of the blade-shaped stepped dropshaft is much less than that of the standard stepped dropshaft. The spacing between the two dotted lines remains approximatively 0.08 independent of Q^*. Accordingly, the flow rate distribution of the blade-shaped stepped
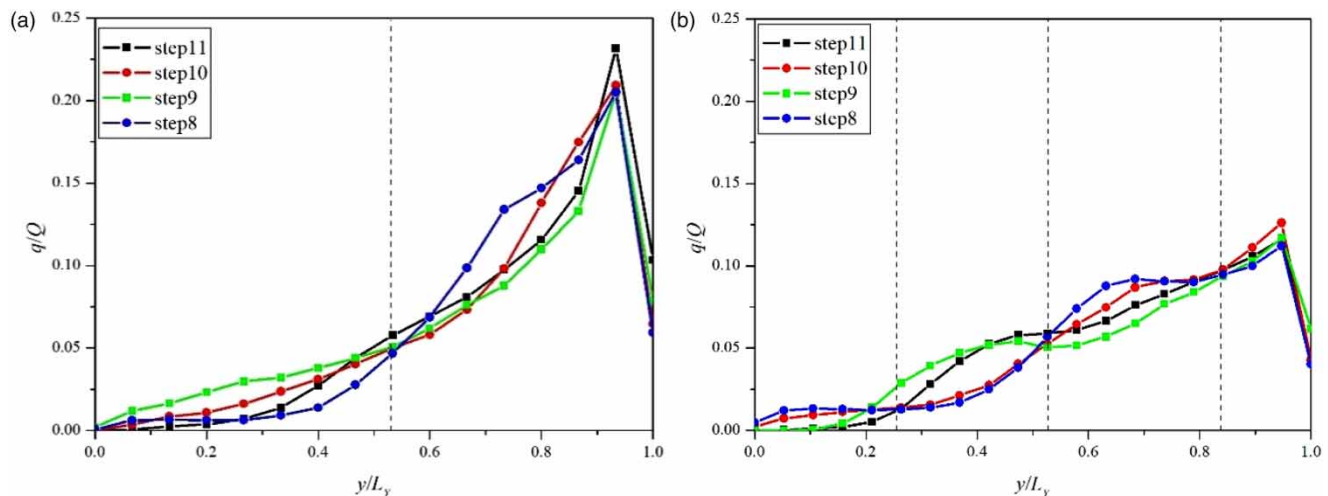

Figure 4 | The flow rate distribution at the end of the step at $Q^* = 0.155$: (a) standard stepped dropshaft; (b) blade-shaped stepped dropshaft.
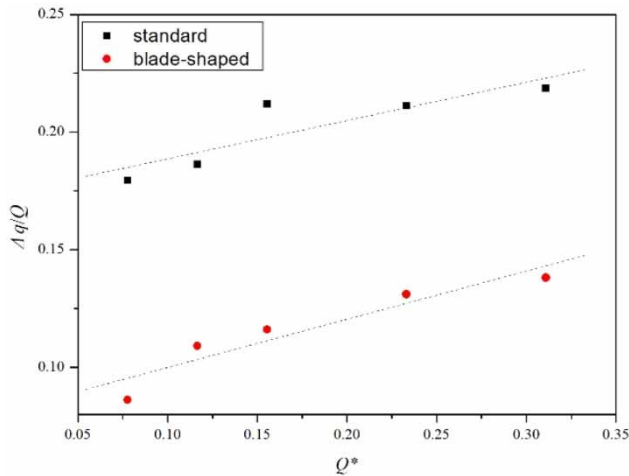
Figure 5 │ The flow rate difference between the internal wall and external wall.

dropshaft is more uniform than that of the standard stepped dropshaft. The reason will be described below via the velocity distribution on the step horizontal surface.

Velocity distribution

Figure 6 shows the velocity distribution on the horizontal step surface for the eighth to the eleventh steps in

both dropshafts at $Q^* = 0.155$. It presents that after the falling jets impact the step, the water breaks up and flows in all directions: one part flows downstream directly; one part flows to the step center; the other first flows in reverse to hit the step vertical wall, then travels to the internal owing to the guidance of the step vertical wall, and finally flows downstream along the internal wall.

The quantity and location of the flow impact points (red circle in Figure 6) can be determined according to the velocity distribution. The curved vertical wall of the step first affects the number and distribution of the impact points, and then affects the distribution of q/Q. For the standard stepped dropshaft, influenced by the centrifugal force, the flow impact points on the step horizontal surface are mainly near the external wall, shown in Figure 6(a). For the blade-shaped stepped dropshaft, several impact points exist on the step center apart from those near the external wall, which leads the flow to the step center and the internal wall, shown in Figure 6(b). Therefore, $\Delta q/Q$ of blade-shaped stepped dropshaft is less than that of the standard stepped dropshaft (Figure 5).
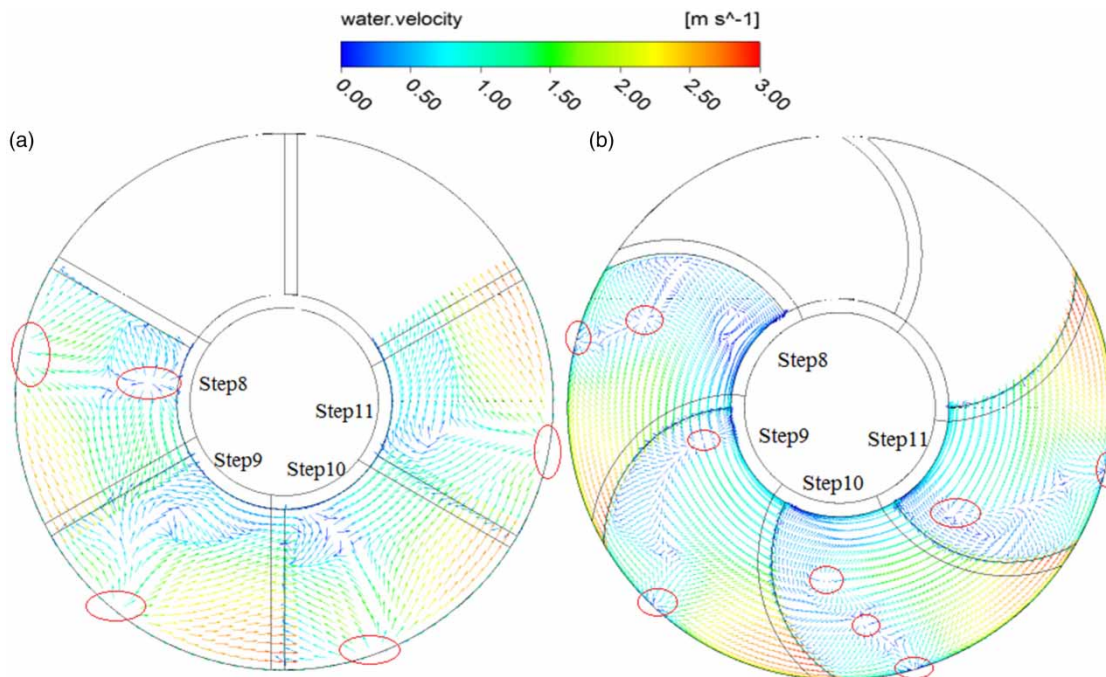

Figure 6 │ Velocity distribution on the step horizontal surface at $Q^* = 0.155$: (a) standard stepped dropshaft; (b) blade-shaped stepped dropshaft.

Time-averaged pressure

Figure 7 presents the time-averaged pressure distribution on the step horizontal surface for the eighth to eleventh steps at $Q^* = 0.078$ and 0.155. The maximum pressure on the step horizontal surface is near the external wall influenced by the impact of main flow. The pressure gradually decreases from the external wall to the internal wall in the radial direction, with a negative pressure zone near the end of the step. It indicates that the time-averaged pressure difference between internal and external increases with the increase of Q^*.
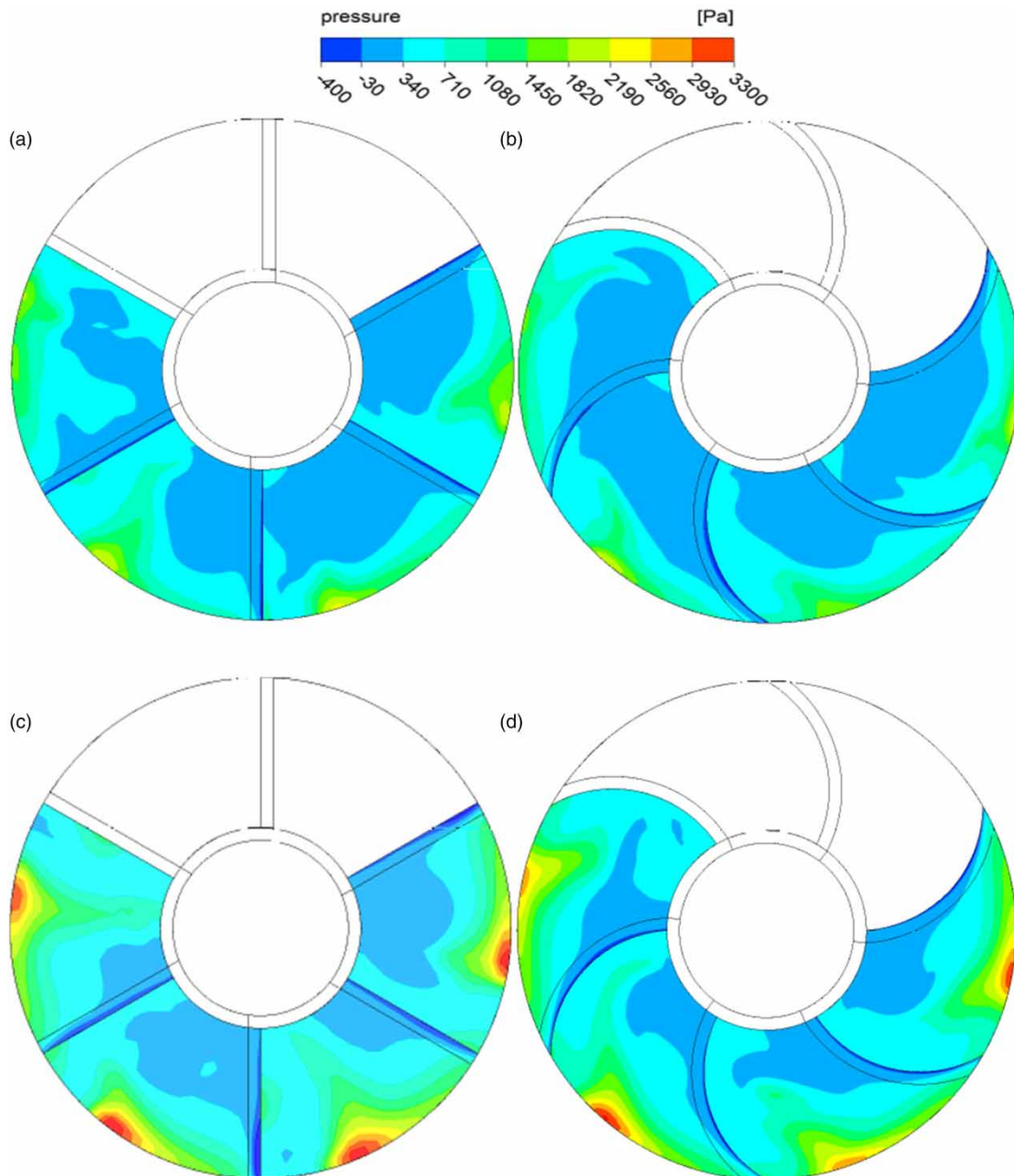
Figure 7 | Time-averaged pressure distribution on the step horizontal surface: (a) and (c) $Q^* = 0.078$ and 0.155 for standard stepped dropshaft; (b) and (d) $Q^* = 0.078$ and 0.155 for blade-shaped stepped dropshaft.

Figure 7(a) and 7(b) present that due to the falling jets step by step, the time-averaged pressure distribution is similar on each step in both stepped dropshafts at $Q^* = 0.078$. Figure 7(c) presents that thanks to the same reason, with the periodic of flow rate distribution, the time-averaged pressure distribution in the blade-shaped stepped dropshaft appears periodic at $Q^* = 0.155$: pressure distribution on the eighth and tenth steps are similar, pressure distribution on the ninth and eleventh steps are similar. Figure 7(d) shows that the time-averaged pressure distribution in the blade-shaped stepped dropshaft is similar on each step, which resulted from the flow skimming over the steps as a coherent stream.

There is an obvious negative pressure zone on each step vertical wall. Figure 8 presents the dimensionless pressure distribution $p_n/\rho gb$ on the negative pressure zone with y/L_Y for the eighth to eleventh steps at $Q^* = 0.155$, where p_n is the vertical average pressure along the water depth. With increasing y/L_Y, $p_n/\rho gb$ first decreases under the influence of the centrifugal force, and then increases near the external wall due to the sidewall resistance. Corresponding to the time-averaged pressure distribution on the step horizontal surface, $p_n/\rho gb$ shows periodic for the standard stepped dropshaft: $p_n/\rho gb$ of the eighth and tenth steps are similar with the minimum $p_n/\rho gb$ at $y/L_Y = 0.67$; $p_n/\rho gb$ of the ninth and eleventh steps are similar with the minimum $p_n/\rho gb$ at $y/L_Y = 0.93$ (Figure 8(a)). For the blade-shaped

stepped dropshaft, $p_n/\rho gb$ from the ninth to eleventh steps are similar, with the minimum $p_n/\rho gb$ at $y/L_Y = 0.68$.

Figure 9 shows the minimum $p_n/\rho gb$ and the dimensionless negative pressure area s/lb, where s is the average negative pressure area for the eighth to eleventh steps vertical walls. It indicates that both $p_n/\rho gb$ and s/lb linearly decrease with the increase of Q^*. With the blade-shaped stepped dropshaft, the minimum $p_n/\rho gb$ are greater and the s/lb are less than that of the standard stepped dropshaft.

Energy dissipation

The energy dissipation η of the dropshaft is expressed as follows:

$$\eta = \frac{E_1 - E_2}{E_1} \tag{15}$$

$$E_1 = Z_1 + \frac{p_1}{\rho g} + \frac{v_1^2}{2g} \tag{16}$$

$$E_2 = Z_2 + \frac{p_2}{\rho g} + \frac{v_2^2}{2g} \tag{17}$$

where E_1 and E_2 are the total energy at the inflow and outflow sections, respectively; Z_1 and Z_2 are the elevation heads of the inlet and outlet channels, respectively; $p_1/\rho g = 0$ and $p_2/\rho g = 0$ are the pressure heads of the inlet
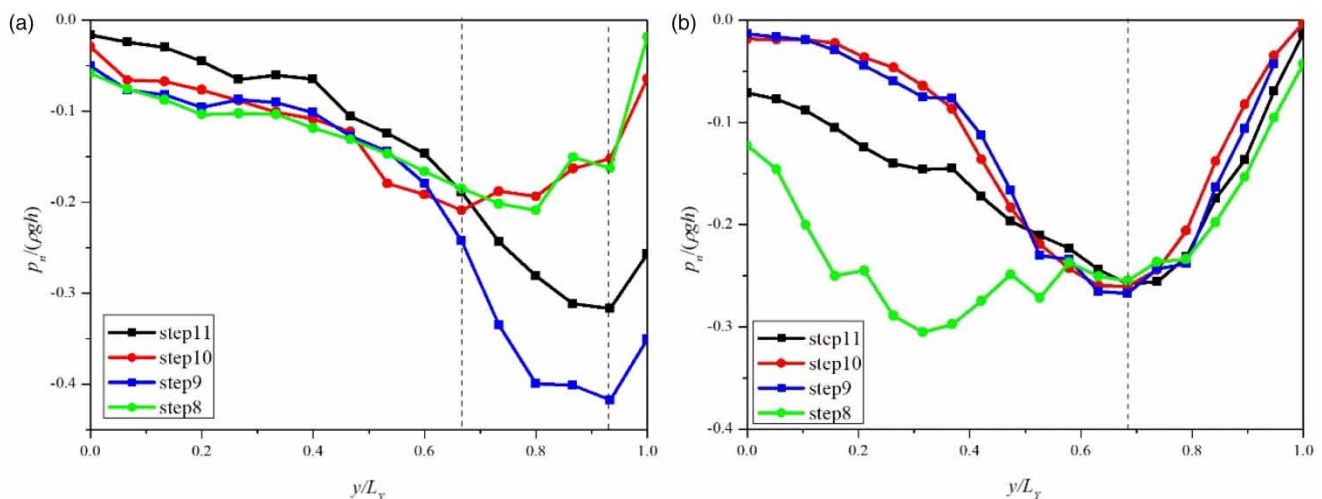

Figure 8 | The negative pressure distribution at $Q^* = 0.155$: (a) standard stepped dropshaft; (b) blade-shaped stepped dropshaft.
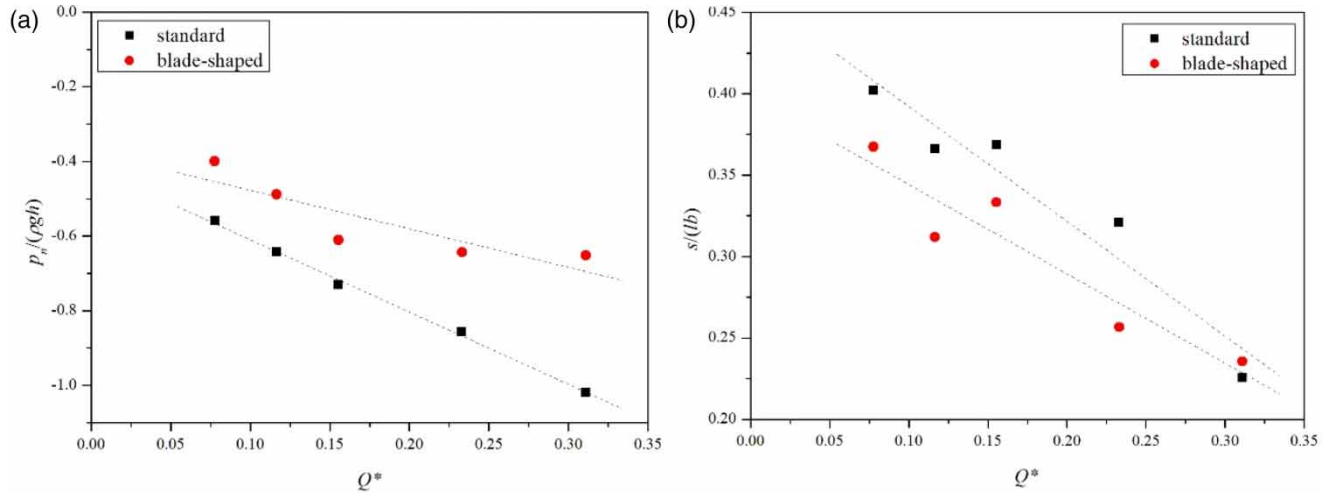
Figure 9 | The minimum $p_n/\rho gb$ and the $s/(lb)$ on the vertical wall: (a) the minimum $p_n/\rho gb$; (b) the s/lb.

and outlet channels, respectively; v_1 and v_2 are the average velocities of the inflow and outflow sections, respectively.

Figure 10 shows the energy dissipation in various dropshafts. The energy dissipation decreases with the increase in the Q^*. The energy dissipation of the standard stepped dropshaft is similar to that of the blade-shaped stepped dropshaft, which indicates that the curved vertical wall of the step has little effect on the energy dissipation. η of the stepped dropshaft in this study agree well with experimental data of the standard stepped dropshaft from Wang (2018), and the

expression of the fitting curve is obtained as:

$$\eta = 0.6689(Q*)^{-0.127} \tag{18}$$

A comparison with the results of a plunging dropshaft (Chanson 2004) indicates that η of the stepped dropshaft is similar to that of the plunging dropshaft in some cases. It is believed that η is related to the multiple parameters of the dropshaft, which is needed further studies.

CONCLUSIONS

In order to control the standing wave and improve the discharge capacity, the blade-shaped stepped dropshaft was proposed in this study to generate a more uniform flow rate distribution in the radial direction by modifying the vertical wall to a curved vertical wall. Three-dimensional numerical simulation was carried out for the hydraulic characteristics of the blade-shaped stepped dropshaft in respect of flow pattern, flow rate distribution, time-averaged pressure and energy dissipation, and the results are compared with the standard stepped dropshaft. The conclusions are summarized as follows:

Compared with the standard stepped dropshaft, the flow rate distribution of the blade-shaped stepped dropshaft was more uniform, with less flow rate difference between the
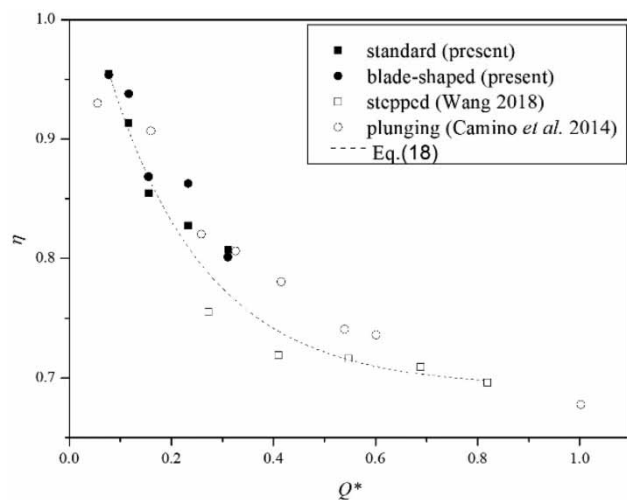

Figure 10 | The energy dissipation in various dropshafts.

internal and external walls at each discharge. Due to the curved vertical wall of the step, more impact points appear on the center of the horizontal step surface, which lead the flow to the internal wall against the centrifugal force. By improving the flow rate distribution in the radial direction, the flow concentration on the external wall and the standing wave can be well controlled.

The numerical simulation results showed that there is a periodic phenomenon of the flow rate distribution and pressure distribution in the stepped dropshaft, which resulted from the flow jumping over the adjacent step and landing on the lower step. Compared with the standard stepped dropshaft, the blade-shaped stepped dropshaft has more uniform pressure distribution on the horizontal step surface and more limited negative pressure on the vertical wall owing to the adjustment of the numbers and locations of the impact points. The energy dissipation of the blade-shaped stepped dropshaft is as high as that of the standard stepped dropshaft, which remains above 0.7 within the range of flow rates.

Based on these findings, it can be found that compared with the standard stepped dropshaft, the blade-shaped stepped dropshaft can improve the discharge capacity, improve the pressure distribution, and keep a good energy dissipation. Therefore, it is a potentially safe and efficient dropshaft design that can be applied to deep tunnel systems.

ACKNOWLEDGEMENTS

DATA AVAILABILITY STATEMENT

All relevant data are included in the paper or its Supplementary Information.

REFERENCES

Ansar, M. & Jain, S. C. 1997 Energy losses in a tangential helicoidal-ramp inlet for drop structures. *Journal of Water Management Modeling* **5**, 223–232.

Changnon, S. A. 2010 Stormwater management for a record rainstorm at Chicago. *Journal of Contemporary Water Research and Education* **146** (1), 103–109.

Chanson, H. 2004 Hydraulics of rectangular dropshafts. *Journal of Irrigation and Drainage Engineering* **130** (6), 523–529.

Cui, F. D., Daskiran, C., King, T., Robinson, B., Lee, K., Katz, J. & Boufadel, M. C. 2020 Modeling oil dispersion under breaking waves. Part I: wave hydrodynamics. *Environmental Fluid Mechanics* **20** (6), 1527–1551.

Guo, Q. & Song, C. C. S. 1990 Surging in urban storm drainage systems. *Journal of Hydraulic Engineering* **116** (12), 1523–1537.

Guo, Q. & Song, C. C. S. 1991 Dropshaft hydrodynamics under transient conditions. *Journal of Hydraulic Engineering* **117** (8), 1942–1955.

Guo, Q., Zhou, L. J., Wang, Z. W., Liu, M. & Cheng, H. 2018 Numerical simulation for the tip leakage vortex cavitation. *Ocean Engineering* **151**, 71–81.

He, Z. J., Wang, B., Yang, Y., Pan, W. W. & Qu, H. 2017 Review on vertical shaft in urban wastewater drainage system. *China Water and Wastewater* **33** (10), 49–53.

Hirt, C. W. & Nichols, B. D. 1981 Volume of fluid (VOF) method for the dynamics of free boundaries. *Journal of Computational Physics* **39**, 201–225.

Kawasaki, S., Mori, Y., Yoshimoto, T. & Nakanishi, T. 1999 Flow characteristics in the helicoidal-ramp dropshaft for middle head. *Ishikawajima-Harima Engineering Review* **39** (6), 309–313.

Kennedy, J. F., Jain, S. C. & Quinones, R. R. 1988 Helicoidal-ramp dropshaft. *Hydraulic Engineering-ASCE* **114** (3), 315–325.

Liao, L., An, R. D., Li, J., Yi, W. M., Liu, X. F., Meng, W. K. & Zhu, L. 2019 Hydraulic characteristics of stepped spillway dropshafts for urban deep tunnel drainage systems: the case study of Chengdu city. *Water Science and Technology* **80** (8), 1538–1548.

Menter, F. R. 1994 Two-equation eddy-viscosity turbulence models for engineering applications. *American Institute of Aeronautics and Astronautics* **32** (8), 1598–1605.

Qi, Y. F., Wang, Y. R. & Zhang, J. M. 2018 Three-dimensional turbulence numerical simulation of flow in a stepped dropshaft. *Water* **11** (1), 1–18.

Qian, S. T. & Wu, J. H. 2020 Hydraulic characteristics of the aeration basin in a ski-jump-step spillway. *Water Supply* **20** (3), 922–929.

Qian, S. T., Xu, H. & Feng, J. G. 2019 Flume experiments on baffle-posts for retarding open channel flow: by C. Ubing, R. Ettema and CI Thornton. Journal of Hydraulic Research 55 (3), 2017, 430–437. *Journal of Hydraulic Research* **57** (2), 280–282.

Rajaratnam, N., Mainali, A. & Hsung, C. Y. 1997 Observations on flow in vertical dropshafts in Urban Drainage Systems. *Journal of Environmental Engineering* **123** (5), 486–491.

Shen, J. Y., Wu, J. H. & Ma, F. 2019 Hydraulic characteristics of stepped spillway dropshafts. *Science China Technological Sciences* **62** (5), 868–874.

Spalart, P. R. & Shur, M. 1997 On the sensitization of turbulence models to rotation and curvature. *Aerospace Science and Technology* **1** (5), 297–302.

Vasconcelos, J. G. & Wright, S. J. 2006 Mechanisms for air pocket entrapment in stormwater storage tunnels. In *World Environmental and Water Resources Congress*.

Vasconcelos, J. G. & Wright, S. J. 2011 Geysering generated by large air pockets released through water-filled ventilation shafts. *Journal of Hydraulic Engineering* **137** (5), 543–555.

Wang, X. C. 2018 *Study on air-Water Two-Phase Flow in Deep Tunnel Drainage System (In Chinese)*. Hohai University.

Wu, J. H., Ren, W. C. & Ma, F. 2017 Standing wave at dropshaft inlets. *Journal of Hydrodynamics, Ser. B* **29** (3), 524–527.

Wu, J. H., Yang, T., Sheng, J. Y., Ren, W. C. & Ma, F. 2018 Hydraulic characteristics of stepped spillway dropshafts with large angle (in Chinese). *Chinese Journal of Hydrodynamics* **33** (2), 176–180.

Wu, J. H., Qian, S. H., Wang, Y. & Zhou, Y. 2020 Residual energy on ski-jump-step and stepped spillways with various step configurations. *Journal of Hydraulic Engineering* **146** (4), 06020002.

Xie, B. & Xiao, F. 2017 Accurate and robust PISO algorithm on hybrid unstructured grids using the multimoment finite volume method. *Numerical Heat Transfer, Part B (Fundamentals)* **71** (2), 146–172.

Zhang, J. Y., Wang, Y. T. & He, R. M. 2016 Discussion on the urban flood and waterlogging and causes analysis in China. *Advances in Water Science* **27** (4), 485–491.